





# Different Formation Scenarios for Counterrotating Stellar Disks in Nearby Galaxies

Min Bao<sup>1,2,3,4</sup>, Yanmei Chen<sup>1,2,3</sup>, Pengpei Zhu<sup>1,2,3,5</sup>, Yong Shi<sup>1,2,3</sup>, Dmitry Bizyaev<sup>6,7</sup> , Ling Zhu<sup>8</sup> , Meng Yang<sup>8</sup>, Minje Beom<sup>9</sup>,Joel R. Brownstein<sup>10</sup> , and Richard R. Lane<sup>11</sup> <sup>1</sup> Department of Astronomy, Nanjing University, Nanjing 210093, People's Republic of China; [chenym@nju.edu.cn](mailto:chenym@nju.edu.cn)<sup>2</sup> Key Laboratory of Modern Astronomy and Astrophysics (Nanjing University), Ministry of Education, Nanjing 210093, People's Republic of China<sup>3</sup> Collaborative Innovation Center of Modern Astronomy and Space Exploration, Nanjing 210093, People's Republic of China<sup>4</sup> School of Physics and Technology, Nanjing Normal University, Nanjing 210023, People's Republic of China<sup>5</sup> Department of Astronomy and Astrophysics, University of California, Santa Cruz, CA 95064, USA<sup>6</sup> Apache Point Observatory and New Mexico State University, P.O. Box 59, Sunspot, NM, 88349-0059, USA<sup>7</sup> Sternberg Astronomical Institute, Moscow State University, Moscow, Russia<sup>8</sup> Shanghai Astronomical Observatory, Chinese Academy of Sciences, 80 Nandan Road, Shanghai 200030, People's Republic of China<sup>9</sup> Department of Astronomy, New Mexico State University, Las Cruces, NM 88001, USA<sup>10</sup> Department of Physics and Astronomy, University of Utah, Salt Lake City, UT 84112, USA<sup>11</sup> Centro de Investigación en Astronomía, Universidad Bernardo O'Higgins, Avenida Viel 1497, Santiago, Chile

Received 2022 January 4; revised 2022 February 6; accepted 2022 February 8; published 2022 February 18

## Abstract

Using the integral field unit data from the Mapping Nearby Galaxies at Apache Point Observatory survey, we select a sample of 101 galaxies with counterrotating stellar disks and regularly rotating ionized gas disks. We classify the 101 galaxies into four types based on the features of their stellar velocity fields. The relative fractions and stellar population age radial gradients of the four types are different in the blue cloud, green valley, and red sequence populations. We suggest different formation scenarios for counterrotating stellar disks; the key factors in the formation of counterrotating stellar disks include (1) the abundance of preexisting gas in the progenitor and (2) the efficiency in angular momentum consumption.

*Unified Astronomy Thesaurus concepts:* [Galaxy kinematics \(602\)](#); [Star formation \(1569\)](#)

## 1. Introduction

The so-called  $2\sigma$  galaxies have two peaks along the major axes of the stellar velocity dispersion fields. A natural explanation is that they host two counterrotating stellar disks (Corsini 2014). Counterrotating disks could form during gas-rich disk-disk mergers (Puerari & Pfenniger 2001; Crocker et al. 2009) or as a result of external gas accretion or gas-rich minor mergers with angular momentum misaligned with the preexisting disk followed by star formation (Thakar & Ryden 1998; Bassett et al. 2017; Khoperskov et al. 2021). These different formation mechanisms will result in different properties of the two disks, including luminosity fraction, stellar population age, and metallicity. The kinematic properties and metallicity of gas in these galaxies provide additional information on their formation scenario.

Since the first discovery of counterrotating stellar disks in NGC 4550 (Rubin et al. 1992), several cases have been studied over the years, e.g., NGC 5719 (Coccatto et al. 2011), NGC 3593 (Coccatto et al. 2013), NGC 4138 (Pizzella et al. 2014), NGC 448 (Katkov et al. 2016), NGC 5102 (Mitzkus et al. 2017), and IC 719 (Pizzella et al. 2018). With high-quality spectra, the absorption lines in these star-star counterrotators feature explicit double peaks. Thus, the two disks could be decomposed through spectra fitting, e.g., Coccatto et al. (2011) and Katkov et al. (2016). With the spectral decomposition method, the surface brightness, stellar velocity, stellar velocity dispersion, age, and metallicity of each disk could be obtained. It turned out that in all these individual cases, the stellar disk,

which is corotating with the gas component, is younger with lower metallicity, indicating that (i) the progenitor obtains counterrotating gas externally; (ii) the newly formed stars inherit the angular momentum from the counterrotating gas, leading to the formation of two counterrotating stellar disks. Bevacqua et al. (2021) selected  $\sim 53$  galaxies with counterrotating stellar disks from about 4000 galaxies in the Mapping Nearby Galaxies at Apache Point Observatory (MaNGA) DR16, finding that in most cases, the gas corotates with the younger disk, which is consistent with studies of individual cases. In addition, Bevacqua et al. (2021) separated their sample into three categories: (1) 11 cases with ongoing star formation, (2) 25 galaxies with multimodality in the stellar populations, and (3) galaxies with unimodality in the stellar populations. They suggested that these different types of galaxies with counterrotating stellar disks have different formation scenarios but did not discuss what these scenarios are.

In this work, we select a sample of 101 galaxies with two counterrotating stellar disks from the MaNGA Product Launch 10 (MPL10; Bundy et al. 2015; Drory et al. 2015; Law et al. 2015, 2016). The sample selection is displayed in Section 2. We classify galaxies with two counterrotating stellar disks into four types in Section 3 and discuss their formation scenarios in Section 4.

## 2. Sample Selection

The data products in this work are drawn from MaNGA MPL10 (Wake et al. 2017; Yan et al. 2016a, 2016b), which includes 9456 unique galaxies. The global  $r$ -band effective radius ( $R_e$ ) defined as the radius that includes the half-light of a galaxy, is adopted from the NASA-Sloan Atlas (NSA; Blanton et al. 2011). The MaNGA observation covers at least to  $1.5 R_e$



Original content from this work may be used under the terms of the [Creative Commons Attribution 4.0 licence](#). Any further distribution of this work must maintain attribution to the author(s) and the title of the work, journal citation and DOI.

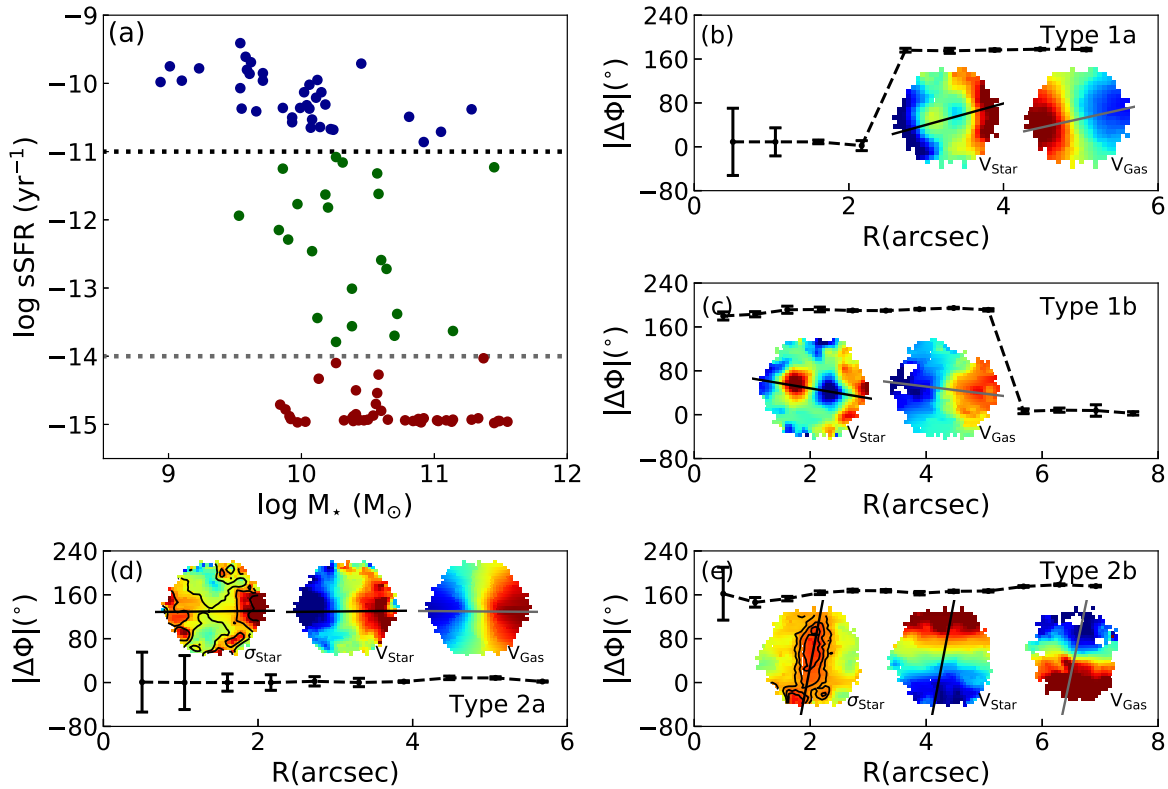


**Figure 1.** (a) Specific star formation rate as a function of stellar mass. The black and gray dotted lines separate galaxies into BC (blue), RS (red), and GV (in between them (green)). (b), (c), (d), (e) The difference in kinematic position angles between the stellar and gas components along the radius (black dashed lines), as well as the stellar and gas velocity fields for Types 1a, 1b, 2a, and 2b CRDs. The black and gray solid lines mark the stellar and gas kinematic major axes. The stellar velocity dispersion fields for Types 2a and 2b are also displayed in panels (d) and (e). The black contours indicate the  $\sigma$  peaks along the stellar major axes.

for most of the targeted galaxies. The spatially resolved properties, i.e., stellar/gas velocity, stellar velocity dispersion, and Lick index 4000 Å break ( $D_n4000$ ), which traces the stellar population age, are obtained from the MaNGA data analysis pipeline (DAP; Westfall et al. 2019). The gas velocity is traced by ionized hydrogen (i.e.,  $H\alpha$ ), while all the emission-line centers are tied together in the velocity space in the MaNGA DAP. We match the MPL10 sample with the literature catalog (Chang et al. 2015) to obtain the global stellar mass ( $M_*$ ) and star formation rate (SFR) for 8431 out of 9456 galaxies and estimate the specific star formation rate as  $sSFR \equiv SFR/M_*$ .

The  $2\sigma$  galaxy was introduced by Cappellari et al. (2011) to describe the feature of off-center but symmetric peaks in the stellar velocity dispersion map along the major axis of a galaxy. Basically, it originates in a galaxy with two counterrotating stellar disks. Considering the prominence of the bulge and the modest spatial resolution of MaNGA, the appearance of one feature does not necessarily imply the other one. Thus, we select galaxies with two counterrotating stellar disks according to one of the following criteria:

1. Search the stellar velocity dispersion fields for two  $\sigma$  peaks or a single elongated  $\sigma$  peak along the major axis: (1) Calculate the mean velocity dispersions along the major and minor axes. (2) Seek galaxies where the velocity dispersion along the major axis is higher than that in the minor axis; we obtained 421 candidates. (3) Visually inspect the stellar velocity dispersion fields of the 421 candidates to make sure there are two  $\sigma$  peaks (see the stellar velocity dispersion map in Figure 1(d)) or a single elongated  $\sigma$  peak (see the stellar velocity

dispersion map in Figure 1(e)) along the major axis. Ninety-nine galaxies are selected.

2. Search the stellar velocity fields for counterrotation between the inner and outer disks. (1) Use the KINEMETRY package (Krajnović et al. 2006) to fit the stellar rotation in each  $0''.5$  (pixel size) ellipse and obtain the position angle. (2) Calculate the position angle differences ( $|\Delta\phi|$ ) between the nearby ellipses, searching for the galaxies that satisfy  $|\Delta\phi| > 150^\circ$ . We obtained 453 candidates. (3) Visually inspect the stellar velocity fields of the 453 candidates for distinguishable counterrotating stellar disks (see the stellar velocity fields in Figures 1(b) and (c)). Thirty-six galaxies are selected.

There are 17 overlaps between the galaxies selected according to the first and second criteria. The other 19 galaxies with counterrotating stellar disks but without off-center  $\sigma$  peaks show low line-of-sight velocities, which can be explained by a low inclination angle (Rubino et al. 2021) or a low intrinsic rotation velocity. In total, we have 118 candidates with counterrotating stellar disks. A few galaxies with counterrotating stellar disks do not show ionized gas emission (Krajnović et al. 2011; Katkov et al. 2016). To clearly assess the gas angular momentum direction and compare it with stars, we exclude 17 galaxies where the gas emission is too weak to be detected or the gas rotation does not have a regular pattern. The final sample applied in the following study consists of 101 galaxies with counterrotating stellar disks and a regularly rotating ionized gas disk. We will refer to them as CRDs in the following sections. Figure 1 shows the sSFR as a function of  $M_*$  for the 101 CRDs. We separate the 101 galaxies into three

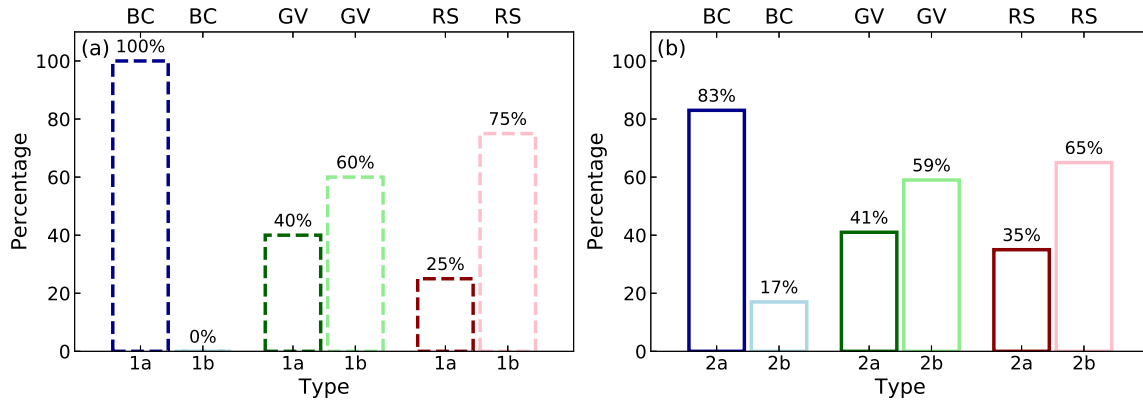


**Figure 2.** (a) The relative contributions of Types 1a and 1b. Blue, green, and red histograms represent the BC, GV, and RS galaxies. The dark-colored dashed-line histograms show the fractions of Type 1a (the gas disk corotating with the inner stellar disk). The light-colored dashed-line histograms show the fractions of Type 1b (the gas disk corotating with the outer stellar disk). (b) The relative contributions of Types 2a and 2b. Blue, green, and red histograms represent BC, GV, and RS galaxies. The dark-colored solid-line histograms show the fractions of Type 2a (star–gas corotators). The light-colored solid-line histograms show the fractions of Type 2b (star–gas counterrotators). The percentage of each type is marked on top of the histogram.

populations: 36 blue cloud (BC) galaxies with  $\log(\text{sSFR}) > -11 \text{ yr}^{-1}$  (blue filled circles in Figure 1(a)), 43 red sequence (RS) galaxies with  $\log(\text{sSFR}) < -14 \text{ yr}^{-1}$  (red filled circles in Figure 1(a)), and another 22 green valley (GV) galaxies in between the two extremes (green filled circles in Figure 1(a)). The spatially resolved BPT diagrams (Baldwin et al. 1981; Kewley et al. 2006) of the 43 RS CRDs show that most of them are dominated by extended low-ionization emission-line regions, i.e., extended LIERs (Belfiore et al. 2016).

### 3. Different Types of Counterrotating Stellar Disks

We classify the sample galaxies into two branches. For the first branch, the counterrotating stellar disks are clearly distinguishable in the stellar velocity fields. This branch can be divided into two types: Types 1a and 1b. Figure 1(b) shows an example of Type 1a. The black dashed line shows the difference in position angles ( $|\Delta\Phi|$ ) between stars and gas along the radius. It is clear the gas disk is corotating with the inner stellar disk and counterrotating with the outer one. Figure 1(c) shows an example of Type 1b where the gas disk is corotating with the outer stellar disk. For the second branch, one of the stellar disks dominates the stellar velocity field; no evidence of two counterrotating stellar disks can be found from the velocity fields, but either the two  $\sigma$  peaks or the single elongated  $\sigma$  peak along the major axis is clearly observed in the stellar velocity dispersion fields. This branch can also be divided into two types: Types 2a and 2b. Figures 1(d) and 1(e) show examples of Types 2a and 2b, respectively. The difference in position angle between the stars and gas indicates star–gas corotation in Type 2a and counterrotation in Type 2b. Corsini (2014) summarized the individual galaxies with a counterrotating stellar disk from earlier literature, and all cases with a regularly rotating ionized gas disk can be included in our classification. Mazzuca et al. (2006) found a ring structure in NGC 7742, where the gas is counterrotating with the stars. We visually inspect the SDSS  $g$ ,  $r$ ,  $i$  color images and  $H\alpha$  flux maps of CRDs and find only three galaxies showing ring structures.

Figure 2(a) shows the relative contributions of Types 1a and 1b in BC (blue), GV (green), and RS (red) galaxies, while the relative contributions of Types 2a and 2b are in Figure 2(b).

From Figure 2(a), we find that 100% of BC galaxies are classified as Type 1a (the gas disk corotates with the inner stellar disk), and this fraction decreases monotonically from BC to 25% in RS galaxies. In contrast, the fraction of Type 1b (the gas disk corotating with the outer stellar disk) increases from BC to RS galaxies. Similarly, in Figure 2(b), 83% CRDs in BC are classified as Type 2a (star–gas corotators), this percentage falls to 41% in GV galaxies and to 35% in RS galaxies, while the percentage of Type 2b (star–gas counterrotators) increases from BC to GV and to RS.

Figure 3 shows the  $D_n4000$  radial gradients in different types of CRDs, with the top row for Type 1 and the bottom row for Type 2. BC, GV, and RS galaxies are shown from the left to right columns, respectively. The blue, green, and red squares/circles mark the median values of  $D_n4000$  in each radial bin for BC, GV, and RS, and the error bars show the 40th to 60th percentiles of the distribution. Considering  $D_n4000$  is a good indicator of the light-weighted stellar population age, Figure 3(a) shows Type 1a CRDs in BC have a young stellar population across the whole galaxy with a slightly positive gradient, indicating the inner disk is slightly younger than the outer disk (Cocato et al. 2013; Mitzkus et al. 2017). In Figure 3(b), the gradients in  $D_n4000$  for Type 1a and Type 1b GV galaxies are totally different, with a positive gradient for Type 1a and negative for Type 1b, indicating Type 1a has a younger inner disk than the outer disk, while the inner disk is older than the outer disk in Type 1b. Although both Types 1a and 1b in RS galaxies (Figure 3(c)) show negative gradients in  $D_n4000$ , indicating the inner disk is older than the outer disk, the slopes of the gradients are clearly different between Types 1a and 1b. Type 1a has a slightly younger (older) stellar population in the central (outer) region than Type 1b. In Figures 3(d), 3(e), and 3(f), negative gradients dominate in Types 2a and 2b (Cocato et al. 2015; Pizzella et al. 2018), except for a flat gradient in Type 2b BC galaxies. It is obvious Type 2a has a younger stellar population than Type 2b in BC, GV, and RS galaxies.

### 4. Formation Scenarios of Counterrotating Stellar Disks

In this work, we select a sample of 101 galaxies with counterrotating stellar disks and classify them into four types based on the features of their stellar velocity fields. As shown

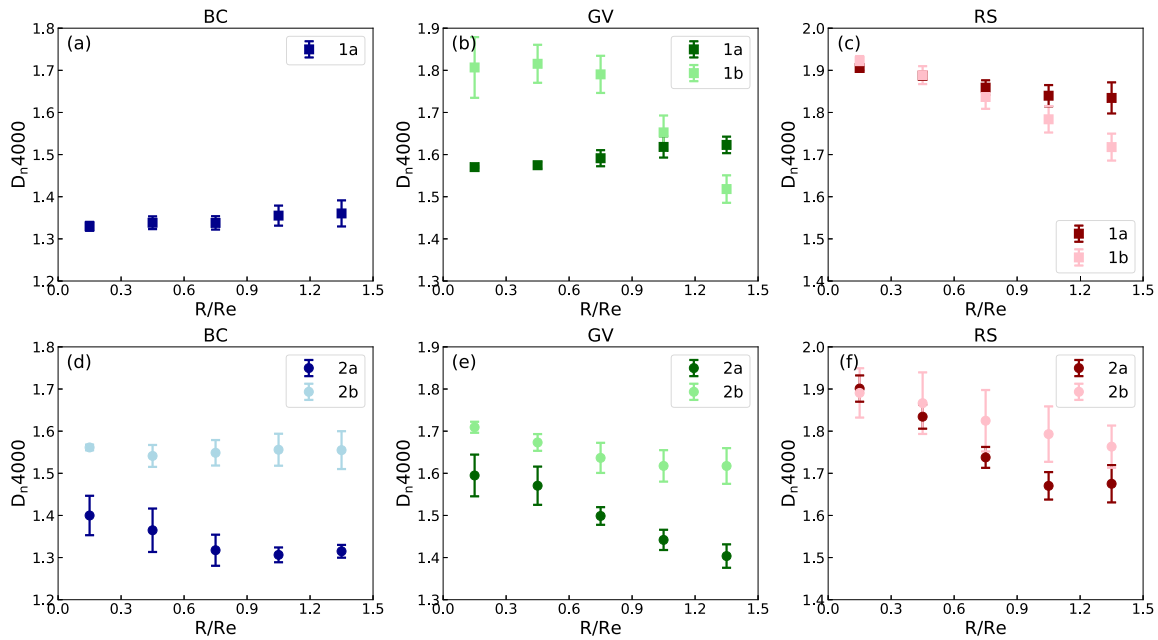


**Figure 3.**  $D_n,4000$  radial gradients in different types of CRDs. Blue, green, and red correspond to the BC, GV, and RS galaxies. (a), (b), and (c) The dark-colored squares mark the median values of  $D_n,4000$  in each radial bin of Type 1a. The light-colored squares mark the median values of  $D_n,4000$  in each radial bin of Type 1b. (d), (e), and (f) The dark-colored circles mark the median values of  $D_n,4000$  in each radial bin of Type 2a. The light-colored circles mark the median values of  $D_n,4000$  in each radial bin of Type 2b. The error bars show the 40th to 60th percentiles of the distribution.

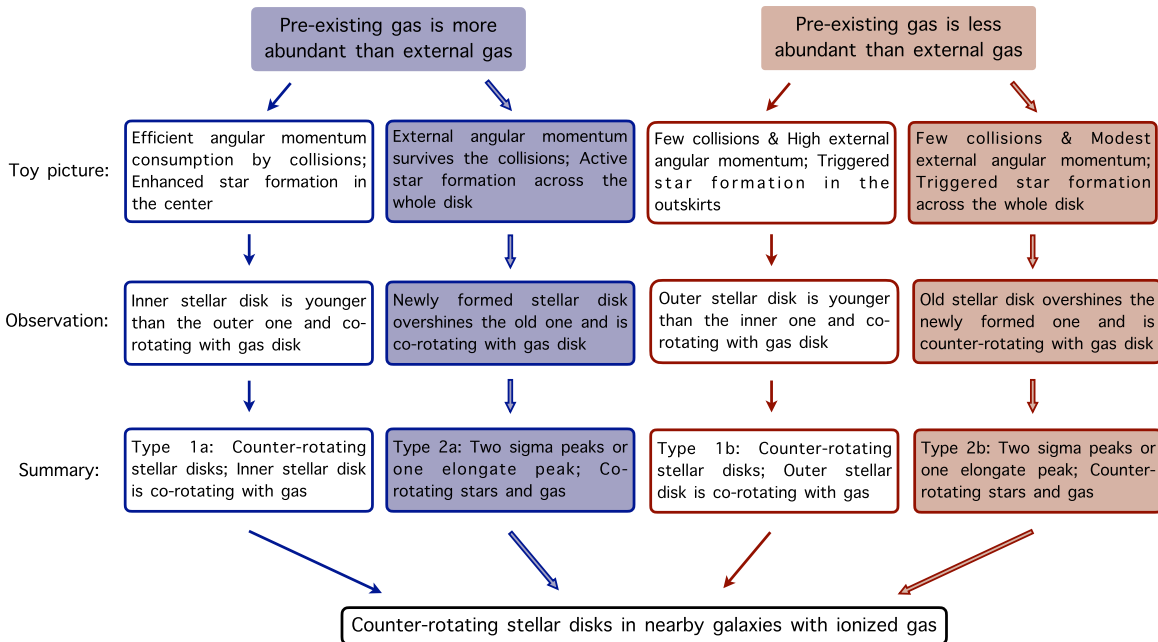


**Figure 4.** Formation scenarios of counterrotating stellar disks in the nearby galaxies with regularly rotating ionized gas disks.

in Figures 2 and 3, the relative fractions of the four types and  $D_n,4000$  radial gradients are different in BC, GV, and RS galaxies, which indicate different formation scenarios of CRDs. We summarize the primary formation scenarios for the four types in Figure 4.

The formation scenarios of Types 1a and 2a CRDs are shown in the first and second columns of Figure 4. In these two types, the gas in progenitors is more abundant than the accreted gas (Pizzella et al. 2004). Collisions between preexisting and external gas efficiently consume the angular momentum in Type 1a, leading to gas inflow and triggering star formation in

the central region. The enhanced star formation in the central region can explain the observations that the inner stellar disk is younger than the outer one in Type 1a BC and GV galaxies (Figures 3(a) and (b)); also, Type 1a has a slightly younger stellar population in the central region than Type 1b RS galaxies (Figure 3(c)). In this case, the inner disk is composed of newly formed stars, which is younger than the outer disk. And the newly formed stars are corotating with the gas where they formed from. Part of the angular momentum of the external gas survives the gas–gas collisions in Type 2a, and the newly formed stars spread over the whole disk, outshine the old

ones. Because the newly formed stars inherit the angular momentum from the gas, gas–star corotation is observed. The monotonically decreasing trends of the Types 1a and 2a fractions from BC to GV and to RS shown in Figure 2 also support the idea that the more abundant the preexisting gas, the higher the efficiency of angular momentum consumption, and the easier it is to form Type 1a and 2a CRDs.

The formation scenarios of Type 1b and 2b CRDs are shown in the third and fourth columns of Figure 4. The preexisting gas is less abundant than the accreted gas, which results in inefficient angular momentum consumption. Thus, star formation in Type 1b is triggered in the outskirts, leading to a younger outer disk corotating with the gas. The younger stellar population in the outskirts of Type 1b compared to that of Type 1a in GV and RS galaxies (Figures 3(b) and (c)) can be explained by this scenario. In Type 2b, the newly formed stars spread over the whole disk, but the star formation is less active than in Type 2a. The old stellar disk, which is counterrotating with the accreted gas, outshines the newly formed ones so that Type 2b has an older stellar population than Type 2a in BC, GV, and RS galaxies (Figures 3(d), (e), and (f)). In Figure 2, the high fractions of Types 1b and 2b in RS galaxies support the idea that poor preexisting gas is preferred in these types of CRDs.

Y.C. acknowledges support from the National Key R&D Program of China (No. 2017YFA0402700), the National Natural Science Foundation of China (NSFC grants 11733002, 11922302), the China Manned Space Project with No. CMS-CSST-2021-A05. M.B. acknowledges support from the National Natural Science Foundation of China (No. 11873032). The authors are very grateful to the referee for valuable comments and suggestions, which improved the work.

Funding for the Sloan Digital Sky Survey IV has been provided by the Alfred P. Sloan Foundation, the US Department of Energy Office of Science, and the Participating Institutions.

SDSS-IV acknowledges support and resources from the Center for High Performance Computing at the University of Utah. The SDSS website is [www.sdss.org](http://www.sdss.org). SDSS-IV is managed by the Astrophysical Research Consortium for the Participating Institutions of the SDSS Collaboration including the Brazilian Participation Group, the Carnegie Institution for Science, Carnegie Mellon University, Center for Astrophysics | Harvard & Smithsonian, the Chilean Participation Group, the French Participation Group, Instituto de Astrofísica de Canarias, The Johns Hopkins University, Kavli Institute for the Physics and Mathematics of the Universe (IPMU) / University of Tokyo, the Korean Participation Group, Lawrence Berkeley National Laboratory, Leibniz Institut für Astrophysik Potsdam (AIP), Max-Planck-Institut für Astronomie (MPIA Heidelberg), Max-Planck-Institut für

Astrofysik (MPA Garching), Max-Planck-Institut für Extraterrestrische Physik (MPE), National Astronomical Observatories of China, New Mexico State University, New York University, University of Notre Dame, Observatório Nacional / MCTI, The Ohio State University, Pennsylvania State University, Shanghai Astronomical Observatory, United Kingdom Participation Group, Universidad Nacional Autónoma de México, University of Arizona, University of Colorado Boulder, University of Oxford, University of Portsmouth, University of Utah, University of Virginia, University of Washington, University of Wisconsin, Vanderbilt University, and Yale University.

## ORCID iDs

Dmitry Bizyaev  <https://orcid.org/0000-0002-3601-133X>

Ling Zhu  <https://orcid.org/0000-0002-8005-0870>

Joel R. Brownstein  <https://orcid.org/0000-0002-8725-1069>

Richard R. Lane  <https://orcid.org/0000-0003-1805-0316>

## References

- Baldwin, J. A., Phillips, M. M., & Terlevich, R. 1981, *PASP*, 93, 5
- Bassett, R., Bekki, K., Cortese, L., et al. 2017, *MNRAS*, 471, 1892
- Belfiore, F., Maiolino, R., Maraston, C., et al. 2016, *MNRAS*, 461, 3111
- Bevacqua, D., Cappellari, M., & Pellegrini, S. 2021, *MNRAS*, 511, 139
- Blanton, M. R., Kazin, E., Muna, D., et al. 2011, *AJ*, 142, 31
- Bundy, K., Bershady, M. A., Law, D. R., et al. 2015, *ApJ*, 798, 7
- Cappellari, M., Emsellem, E., Krajnović, D., et al. 2011, *MNRAS*, 416, 1680
- Chang, Y.-Y., van der Wel, A., da Cunha, E., et al. 2015, *ApJS*, 219, 8
- Coccatto, L., Fabricius, M., Morelli, L., et al. 2015, *A&A*, 581, A65
- Coccatto, L., Morelli, L., Corsini, E. M., et al. 2011, *MNRAS*, 412, L113
- Coccatto, L., Morelli, L., Pizzella, A., et al. 2013, *A&A*, 549, A3
- Corsini, E. M. 2014, in ASP Conf. Ser. 486, Multi-Spin Galaxies, 486, ed. E. Iodice & E. M. Corsini (San Francisco, CA: ASP), 51
- Crocker, A. F., Jeong, H., Komugi, S., et al. 2009, *MNRAS*, 393, 1255
- Drory, N., MacDonald, N., Bershady, M. A., et al. 2015, *AJ*, 149, 77
- Katkov, I. Y., Sil'chenko, O. K., Chilingarian, I. V., et al. 2016, *MNRAS*, 461, 2068
- Kewley, L. J., Groves, B., Kauffmann, G., et al. 2006, *MNRAS*, 372, 961
- Khoperskov, S., Zinchenko, I., Avramov, B., et al. 2021, *MNRAS*, 500, 3870
- Krajnović, D., Cappellari, M., de Zeeuw, P. T., et al. 2006, *MNRAS*, 366, 787
- Krajnović, D., Emsellem, E., Cappellari, M., et al. 2011, *MNRAS*, 414, 2923
- Law, D. R., Cherinka, B., Yan, R., et al. 2016, *AJ*, 152, 83
- Law, D. R., Yan, R., Bershady, M. A., et al. 2015, *AJ*, 150, 19
- Mazucca, L. M., Sarzi, M., Knapen, J. H., et al. 2006, *ApJL*, 649, L79
- Mitzkus, M., Cappellari, M., & Walcher, C. J. 2017, *MNRAS*, 464, 4789
- Pizzella, A., Corsini, E. M., Vega Beltrán, J. C., et al. 2004, *A&A*, 424, 447
- Pizzella, A., Morelli, L., Coccatto, L., et al. 2018, *A&A*, 616, A22
- Pizzella, A., Morelli, L., Corsini, E. M., et al. 2014, *A&A*, 570, A79
- Puerari, I., & Pfenniger, D. 2001, *Ap&SS*, 276, 909
- Rubin, V. C., Graham, J. A., & Kenney, J. D. P. 1992, *ApJL*, 394, L9
- Rubino, M., Pizzella, A., Morelli, L., et al. 2021, *A&A*, 654, A30
- Thakar, A. R., & Ryden, B. S. 1998, *ApJ*, 506, 93
- Wake, D. A., Bundy, K., Diamond-Stanic, A. M., et al. 2017, *AJ*, 154, 86
- Westfall, K. B., Cappellari, M., Bershady, M. A., et al. 2019, *AJ*, 158, 231
- Yan, R., Bundy, K., Law, D. R., et al. 2016a, *AJ*, 152, 197
- Yan, R., Tremonti, C., Bershady, M. A., et al. 2016b, *AJ*, 151, 8